Synthesis and Characterization of Individual High-Entropy Alloy Particles for Electrocatalytic Water Oxidation

Muhammad Rauf,[†] Gaukhar Askarova,[†,§] Tianyu Bo, [†,§] and Michael V. Mirkin[†,#,]*

[†] *Department of Chemistry and Biochemistry, Queens College, Flushing, NY 11367, USA*

[§] *The Graduate Center of CUNY, New York, NY 10016*

[#] *Advanced Science Research Center at The Graduate Center, CUNY; New York, NY 10031*

Corresponding Author

E-mail: mmirkin@qc.cuny.edu

Abstract

High-entropy alloys (HEAs) have attracted considerable attention as promising catalysts. Despite a rapidly growing number of publications in this area, characterization of HEA electrocatalytic activity and stability remains challenging. In this paper, we report rapid and scalable microwave-shock assisted synthesis of FeCoNiCuMnCr HEA and its characterization at a single particle level. HEA particles synthesized on HOPG without additional reagents or pre-/post-treatments exhibited a significant activity toward water oxidation in 0.1 M NaOH. Individual micrometer-sized FeCoNiCuMnCr HEA particles were imaged by scanning electron microscopy/energy dispersive X-ray spectroscopy (SEM/EDS) to show the uniform distribution of all six metals, and the potential dependence of the oxygen evolution reaction (OER) at its surface was probed by scanning electrochemical microscopy (SECM). Significant variations in onset potential of OER on different HEA particles were observed; however, no obvious correlation with the particle size was found. The HEA stability was confirmed by SEM/EDS imaging of the same FeCoNiCuMnCr particle after several hours of OER experiments and also by voltammetry and XRD analysis.

KEYWORDS: high-entropy alloy, microwave synthesis, scanning electrochemical microscopy, oxygen evolution reaction, electrocatalysis

1. Introduction

High entropy alloys (HEAs) are an emerging class of materials composed of five or more metallic elements.[1] They have potentially useful applications in catalysis and energy storage due to their advantageous physicochemical properties.[2-4] The key aspect of HEAs is the vastness of compositional configurations of elements that form homogenized crystalline solid-solution phases by high mixing entropy.[5-7] Furthermore, HEAs exhibit a mixing effect, resulting in synergistic responses from the mutual electronic interactions between multiple compositional elements.[2,8,9] The availability of multimetallic active sites on HEA surfaces also makes them suitable as catalysts for various technologically important electrochemical processes.[9-14]

HEA synthesis presents significant challenges.[15] HEA particles are typically produced using conventional wet chemistry techniques involving chemical reductions and furnace heating protocols.[16-18] These approaches are often plagued by elemental phase separation because many metallic elements are immiscible under thermodynamic equilibrium conditions.[19,20] Mixing five or more elements typically demands heating to extremely high temperatures followed by rapid cooling at rates greater than 10^3 K/s to effectively maintain the nonequilibrium state.[21,22] To overcome thermodynamic limitations, flash heating/cooling methods not based on conventional furnaces are being developed to synthesize multi-metallic alloys.[21-24] Yao et al. synthesized HEA particles with a two-step carbothermal shock technique.[22] This method employs flash heating and cooling, applying a high temperature (>2000 K) to produce uniform and monodisperse HEA particles on electrically conductive materials. The scalability of the carbothermal shock approach is limited by attainable geometrical area of the conductive substrate. The main issues are the efficiency of heating and the nonuniform heat distribution over a large carbon nanofiber substrate.[25] Another approach

is microwave heating – a highly effective technique for generating thermal energy, which has been utilized for scaling up the HEA synthesis.[26]

HEA particles on conductive support are actively investigated as promising oxygen evolution reaction (OER) catalysts as they offer several parameters for optimizing the electronic structure and catalytic sites, which is essential for complicated and sluggish $4e^-$ OER.[11,17,27-29] One can increase the OER efficiency by including precious metals (e.g., Ir, Ru, Pd) in HEA catalysts to lower the energy barrier.[30-32] For instance, IrFeCoNiCu HEA nanoparticles (NPs) exhibited excellent activity for OER in acidic solution with an overpotential of ~302 mV measured at 10 mA cm^{-2}.[11] The same elemental combination also showed a significant OER activity in an alkaline environment.[33] The Rossmeisl group experimentally explored the composition space of the high entropy oxide with 8-elements (AuIrOsPdPtReRhRu) for the OER and performed complementary DFT modeling of the IrOsPdPtRhRu subspace.[34] In ref. 35, Ru-doped FeCoNiXRu (X: Cu, Cr, and Mn) HEAs system was synthesized and studied to understand the correlation between specific active sites and intermediates in multistep electrochemical reactions. The high cost and limited availability of precious metals, such as Ir and Ru, drive the efforts to replace them with much cheaper earth-abundant elements.[36-39] For example, CrMnFeCoNi HEA NPs exhibited high OER catalytic activity with an overpotential of 265 mV at the current density of 10 mA/cm^2 in alkaline media.[40] The DFT calculations showed the incorporation of Cr within the defective HEA structure that reduces the energy barrier for the generation of *OOH from *O and the release of O_2. A copper-rich CuNiFeCrCo alloy was deposited on Ni foam as HER and OER catalyst with a low onset potential of 240 mV vs RHE for the OER.[41]

Two types of instabilities – structural and chemical – have been observed in HEA electrocatalysts in alkaline or acidic solutions. HEA particles may undergo phase transformations due to changes in their composition.[11,42] HEAs containing precious metals

were reported to better maintain their microstructure,[43] while non-precious HEAs exhibited more significant changes during OER, potentially leading to their gradual degradation.[44] Chemical instability, including HEA oxidation, can be induced by electrolytic environment, pH, and applied potential.[43,45] Song et al. reported that the 3d metals are easily oxidized due to their higher chemical activity.[46] HEAs containing precious metals (e.g., Ir) tend to be chemically stable[11] unlike non-precious-metal HEAs whose electrochemical stability varies significantly and may require protection to avoid oxidation or dissolution.[43,47]

Characterizing and benchmarking the activity of HEA electrocatalysts is challenging due to the unknown total surface area and heterogeneity of HEA particles whose size may range from nanometers to micrometers.[48] In published HEA studies, the current density is typically reported per surface area of the conductive support rather than the true surface area of the catalyst. Moreover, the total measured current may contain contributions from parallel processes, including HEA dissolution and/or oxidation, which are hard to separate from that of the OER or another electrocatalytic process of interest. These difficulties can be alleviated by using scanning electrochemical microscopy (SECM) to probe individual HEA particles.

SECM[49-52] and scanning electrochemical cell microscopy (SECCM)[53,54] have previously been employed to map and quantify localized activities of multimetallic catalytic systems, including HEAs. SECM has been extensively used to characterize reactivity of electrocatalysts by scanning the tip electrode across the catalyst surface and measuring the local fluxes of reactants and products.[55] Most of those experiments were carried out with micrometer-sized SECM tips, which did not provide sufficiently high spatial resolution to probe catalytic activity at the single particle level. Here, we use nanoSECM to measure the flux of oxygen produced at an individual HEA particle at different applied potentials. The negative feedback mode of SECM (Fig. 1A) was used to locate a single HEA particle on the HOPG surface. Dioxygen dissolved in solution was reduced at the tip, and the tip potential (E_T) was such that the tip

current (i_T) was only due to the ORR at its surface, while the substrate was unbiased. When the separation distance between the tip and substrate (d) was small (i.e., comparable to the tip radius, a), i_T decreased with decreasing d because of the hindered O_2 diffusion (negative feedback; the tip current near the surface is lower than in the bulk solution; $i_T < i_{T,\infty}$) since no oxygen regeneration occurred on the substrate. The substrate generation/tip collection (SG/TC) mode (Fig. 1B) was then used to assess the HEA activity towards OER. The tip collected oxygen produced by water oxidation on the positively biased substrate surface. The changes in i_T with d, in this case reflect the competition between two opposing effects – generation of oxygen at the substrate and hindered diffusion of dissolved O_2 from the bulk solution to the tip surface. The tip current was recorded either as a function of d (approach curve) or tip x–y position (imaging).

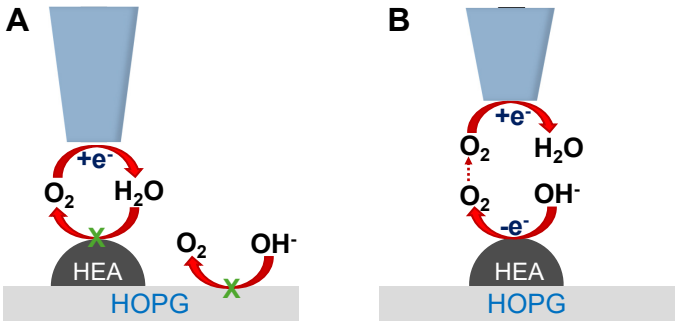

Fig. 1. (A) Negative SECM feedback produced by blocking of oxygen diffusion to the tip by an unbiased HEA particle and (B) SG/TC measurement of OER on a positively biased HEA particle.

In this Article, we synthesize HEA particles from first-row transition metals (Fe, Co, Ni, Mn, Cr, and Cu) on highly oriented pyrolytic graphite (HOPG) support *via* decomposition of precursor materials at high temperatures created by microwaving, and subsequent rapid cooling.[26] SECM is used to directly probe the oxygen flux generated on individual HEA particles at different potentials, separate OER from parallel processes occurring at the HEA surface, and demonstrate the heterogeneity of the particle catalytic activity. To relate the SECM

data to HEA stability and compositional uniformity, the same particles were imaged by scanning electron microscopy (SEM) and mapped by energy dispersive X-ray spectroscopy (EDS) before and after electrochemical experiments.

2. Results and Discussion

We used a straightforward and controlled microwave-assisted shock method to synthesize FeCoNiCuMnCr HEA particles supported on HOPG (for details, see Experimental section). Rapid heating and quenching by microwave irradiation have previously been used for synthesizing micro- and nano-scale single-phase alloyed structures.[11,20,26,56,57] During microwave irradiation, the carbon paper (Toray 060) on the HOPG substrate absorbed electromagnetic energy and converted it into thermal energy to generate a high temperature within several seconds, and the sample emitted bright light due to black-body radiation.[58] The high temperature caused thermal decomposition of the transition metals precursors and the formation of HEA particles on the HOPG substrate (HEA/HOPG). The rapid increase in temperature inhibits aggregation of the produced HEA particles distributed on the HOPG support. The attachment of HEA particles to the substrate surface was strengthened by annealing the sample at 300 ℃. HOPG is a good support for HEA because of its catalytic inertness, high thermal conductivity, and stability under microwave irradiation (Fig. S2).

2.1 HEA characterization and elemental composition analysis

The topography and composition of the synthesized HEAs particles were characterized by SEM-EDS. Fig. S1 shows an SEM image of the HEA/HOPG sample, which consists of particles with the size ranging from 2 to 35 μm distributed on the HOPG surface. An SEM image of the 29-μm-diameter HEA particle, which was selected for SECM studies, is shown in Fig. 2A. The uniform distribution of all six elements, i.e., Fe, Co, Ni, Cu, Mn, and Cr, within the same HEA particle can be seen in Figs. 2B-2G. The single-phase alloy structure of FeCoNiCuMnCr HEA particles was confirmed by SEM-EDX elemental mapping overlay in

Fig. 2H. Fig. S7 presents SEM/EDS maps of a smaller (~8 µm diameter) HEA particle on the HOPG surface, confirming its compositional uniformity.

The EDX elemental analysis was employed to determine the atomic ratios of all metal elements (Table S1) in the ensemble of HEA particles. The measured atomic ratios are close to those expected from the chemical formula of HEA (FeCoNiCuMsnCr). Importantly, this HEA was produced without using surfactants or structural templates, thus eliminating extra steps required to remove these structure-directing reagents and reducing structural damage.

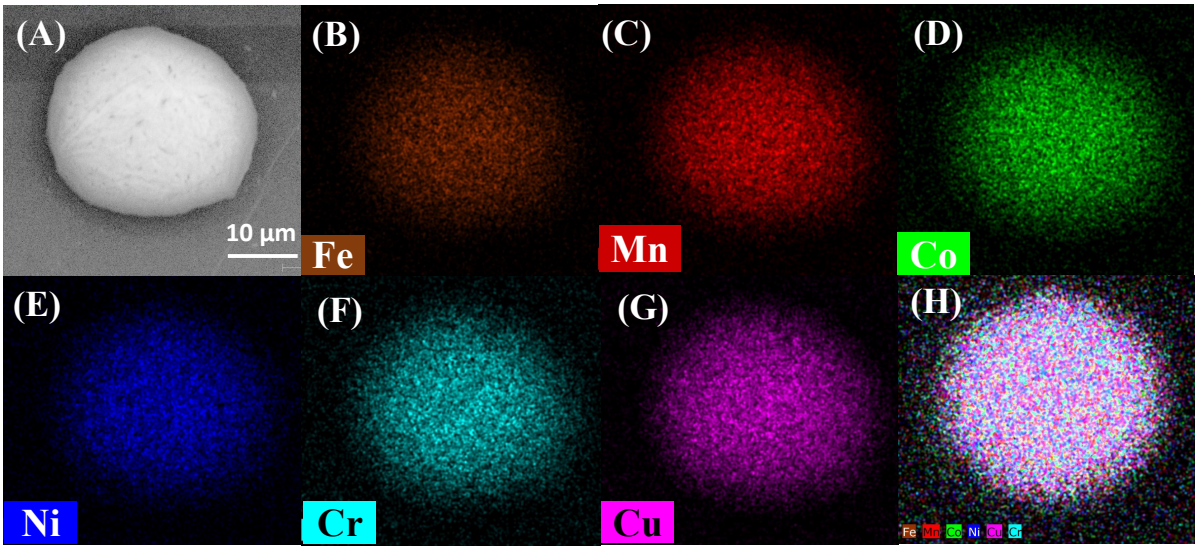

Fig. 2. SEM-EDS of as-synthesized FeCoNiCuMnCr HEA/HOPG sample using secondary electron (SE) detector. (A) SEM image of an individual HEA particle, (B-G) EDS elemental mapping of the same particle, and (H) the overlay of the maps shown in panels B - G.

The crystal structures of the HOPG and synthesized HEA were analyzed using X-ray diffraction (XRD). XRD patterns of bare HOPG (Fig. 3A) comprise three diffraction peaks, (002), (004), and (006), corresponding to the angle values $2\theta \approx 26.5°$, 54.6°, and 86.9°, in which the (002) peak associated with [002] plane of graphite carbon according to PDF#56-0159 exhibits the highest diffraction intensity.[59] XRD patterns of FeCoNiCuMnCr/HOPG before electrochemical measurements (Fig. 3B; high HOPG-related peaks, which obscure the HEA signal, have been removed from this figure) contain three main diffraction peaks at

2θ = 41.5°, 49.6° and 77°, which can be indexed to the (111), (200), and (220) planes of the fcc phases, according to PDF#26-4164, respectively.[35] No separate XRD peaks of Fe, Co, Ni, Mn, Cu, Cr or metal oxides were observed, suggesting the formation of the single-phase HEA. Compared to the standard diffraction patterns of the cubic FeCoNi alloy (PDF#26-4164), the fcc diffraction peaks of the FeCoNiCuMnCr HEA shifted slightly to lower angles. This shift can be attributed to lattice distortions caused by the incorporation of Cr and Mn atoms, which contribute to the high entropy of the alloy. The larger atomic radii of Cr and Mn, compared to Fe, Co, Cu, and Ni, are likely responsible for these distortions.[40]

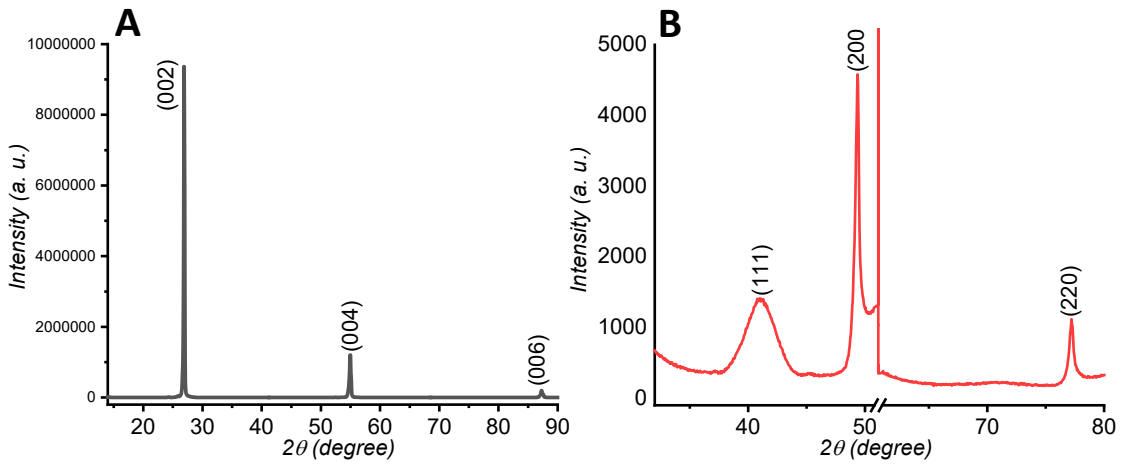

Fig. 3. XRD patterns of bare HOPG (A) and FeCoNiCuMnCr HEA particles on HOPG (B).

2.2 Bulk OER voltammetry at HEA particles

Voltammograms of OER at the ensemble of FeCoNiCuMnCr HEA particles immobilized on an HOPG electrode were obtained in an alkaline (pH 13) solution. Two linear sweep voltammograms (LSVs; Fig. 4) were recorded in Ar-saturated 0.1 M NaOH at a scan rate, v = 5 mV/s. An LSV obtained at the HEA/HOPG (red curve in Fig. 4) shows the water oxidation current much higher than that measured at the bare HOPG (black curve) and an onset potential of ~0.45 V vs. Ag/AgCl on the FeCoNiCuMnCr HEA particles. This value is about 80 mV lower than that observed previously for a precious metal-doped HEA (FeCoNiCuIr).[32] The activity of our HEA particles is augmented by homogeneous distribution of each

component without any phase separation (Fig. 2), whereas it was previously noted that a nonuniform structure of the electrocatalyst decreases its electroactivity via a reduced number of accessible active sites.[40] Quantitative comparison of the HEA catalytic activity to the literature results of bulk measurements is difficult because of the size heterogeneity and unknown total surface area of the particles.

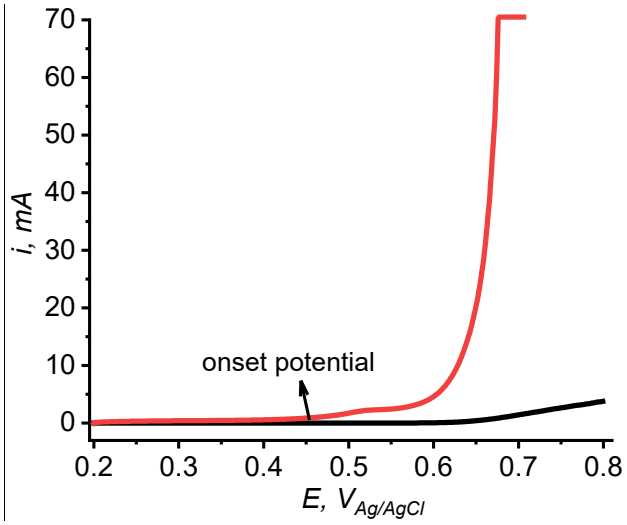

Fig. 4. LSVs of OER at HEA/HOPG (red curve) and bare HOPG electrode (black curve) in 0.1 M NaOH. v = 5 mV/s.

2.3 Probing OER activity of single HEA particles by SECM

SECM was used to probe the flux of oxygen generated by water oxidation on the HEA particle imaged in Fig. 2. A Pt nanoelectrode was biased at a sufficiently negative potential to solely drive ORR on its surface. Initially, the negative feedback mode (Fig. 1A) was employed to position the tip above the center of the particle and establish the tip/substrate separation distance (Fig. S3). Subsequently, in SG/TC mode, the substrate was biased positively to induce water oxidation on HEA particles in pH 13 solution, while the tip was kept at a negative bias to collect generated oxygen (Fig. 1B). Fig. 5A shows four approach curves recorded with the substrate potential, E_S of 0.2 V (curve 1), 0.3 V (curve 2), 0.4 V (curve 3), and 0.6 V (curve 4) vs. Ag/AgCl. At E_S = 0.2 V, the flux of generated oxygen above the HEA particle was very small, resulting in the slight decrease in i_T at shorter d due to blocking of the O_2 diffusion to

the tip by the substrate surface (curve 1). At E_S = 0.3 V (curve 2), the tip current slightly increased with decreasing d, and the i_T at longer distances was significantly higher than the corresponding values in curve 1, pointing to the generation of oxygen at the particle. The flux of generated O_2 continued to increase with E_S (curves 3 and 4). A similar dependence of i_T on E_S can be seen in four LSVs (Fig. 5B) recorded at the same tip that was held near the surface of the same particle. At E_S = 0.2, the ORR voltammogram at the tip corresponds to the reduction of O_2 dissolved in solution (curve 1 in Fig. 5B). The higher i_T at more positive substrate potentials (curves 2 – 4) are due to larger oxygen flux generated at the HEA particle.

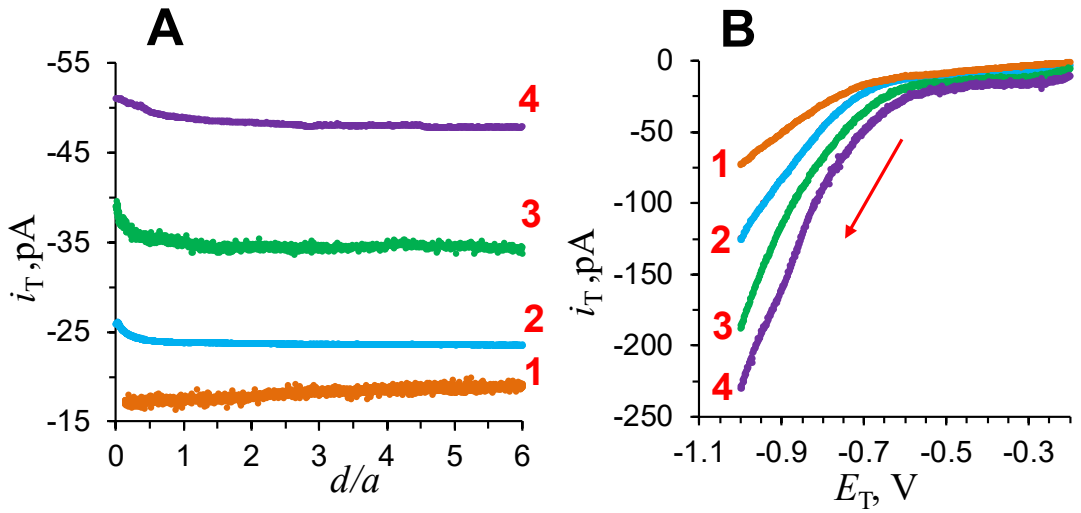

Fig. 5. (A) SECM current-distance curves recorded with a Pt tip approaching a 14.5-µm-radius HEA particle on HOPG substrate and (B) LSVs of ORR recorded at the same tip positioned near the surface of the same particle. E_s, V *vs.* Ag/AgCl = 0.2 (1), 0.3 (2), 0.4 (3), and 0.6 (4). a = 355 nm; RG = 1.1; solution contained 0.1 M NaOH. (A) E_T = −0.7 V. (B) v = 0.1 V/s; red arrow indicates the scan direction.

From Fig. 5A, the OER onset potential is between 0.2 V and 0.3 V vs. Ag/AgCl. This value is about 200 mV lower than the apparent onset in Fig. 4. This difference points to heterogeneity in the electrocatalytic activity of HEA particles for OER; however, the onset potential estimate from Fig. 4 is not highly accurate because of a significant background current. Further evidence for catalytic heterogeneity of HEA particles can be seen is Fig. S4, where the i_T *vs* E_S curve recorded with a nanotip held at a constant potential, E_T = -0.7 V and d = 85 nm

from a 50-µm-radius HEA particle shows a much higher onset potential of ~0.7 V vs Ag/AgCl (*cf.* Fig. 5). We also mapped a much smaller (~500 nm radius) HEA particle by SECM and obtained OER-based approach curves (Fig. S8). The OER onset potential for this particle is very similar to the value obtained for a 14.5-µm-radius particle (Fig. 5), suggesting that the particle size may not be a major factor determining its activity for OER.

The rate of the OER at different substrate potentials was evaluated by fitting experimental approach curves (symbols in Figs. 6A and 6B) to the theoretical curves (red solid lines) generated by finite element simulations (see COMSOL simulation report in Supporting Information). An oxygen flux, f_{O2} = 2.6 nmol cm^{-2} s^{-1} was generated at E_s = 0.7 V (B), and a

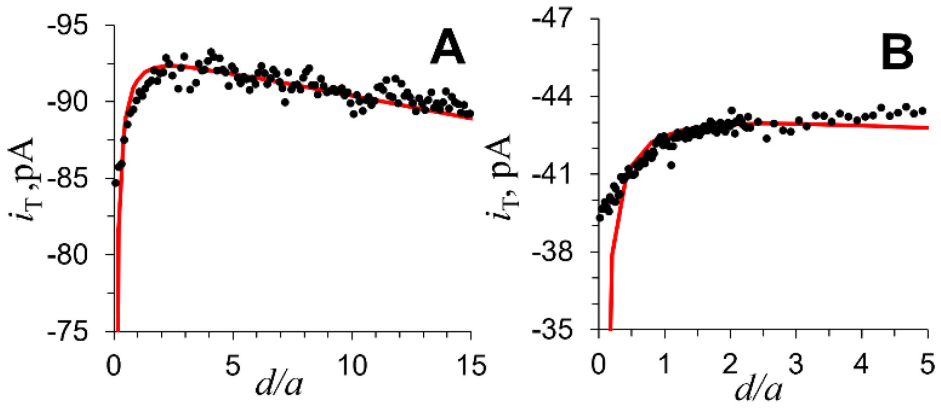

Fig. 6. Experimental $i_T - d$ curves (black symbols) obtained with a Pt tip approaching a 50-µm-radius HEA particle biased at E_s = 0.8 V (A) and 0.7 V (B) *vs*. Ag/AgCl. Theoretical fitting curves (red solid line) were calculated for a = 200 nm and RG = 1.5. $i_{T,\infty}/i_{T,d}$ = 0.06 (k_T = 0.123 cm/s), and f_{O2} = 7 nmol cm^{-2} s^{-1} (A) and 2.6 nmol cm^{-2} s^{-1} (B). Solution contained 0.1 M NaOH. E_T = −0.9 V *vs.* Ag/AgCl.

significantly larger flux of 7 nmol cm^{-2} s^{-1} was produced by the same HEA particle at 0.8 V vs. Ag/AgCl (A). These values correspond to the OER current density of ~1 mA/cm^2 and ~3 mA/cm^2 at the overpotential of 0.45 V and 0.55 V, respectively ($E^{o'}_{O_2/H_2O}$ = 0.253 V vs. Ag/AgCl at pH 13 [60]).

2.4 Assessing HEA stability through SEM imaging after electrochemical experiments

To assess structural and chemical stability of HEA/HOPG sample, the same

FeCoNiCuMnCr particle was imaged by SEM-EDS before (Fig. 2) and after (Fig. 7) electrochemical experiments. The comparison of SEM images (Fig. 2A and Fig. 7A) shows no appreciable change in particle size and geometry after several-hour-long voltammetric and SECM measurements. The HEA particle also preserved the characteristic homogeneous elemental distribution without noticeable phase separation or elemental segregation (*cf.* Figs. 2B-2H and Figs. 7B-7H). To be suitable for SECM experiments, the selected HEA particle had to be relatively large and could not be imaged by TEM. The possibility of metal oxide formation during electrocatalytic water oxidation could not be checked because of the limited spatial resolution in Figs. 2 and 7 and the lack of oxidation state characterization. However, the XRD pattern of HEA/HOPG recorded after several hours of electrochemical experiments (Fig. S5) to assess the stability of the HEA crystalline structure is very similar to that of the original sample (Fig. 3B) with no additional peaks corresponding to Fe, Co, Ni, Mn, Cu, Cr, or metal oxides. This data, consistent with the EDX analysis, confirms the structural stability of the HEA.

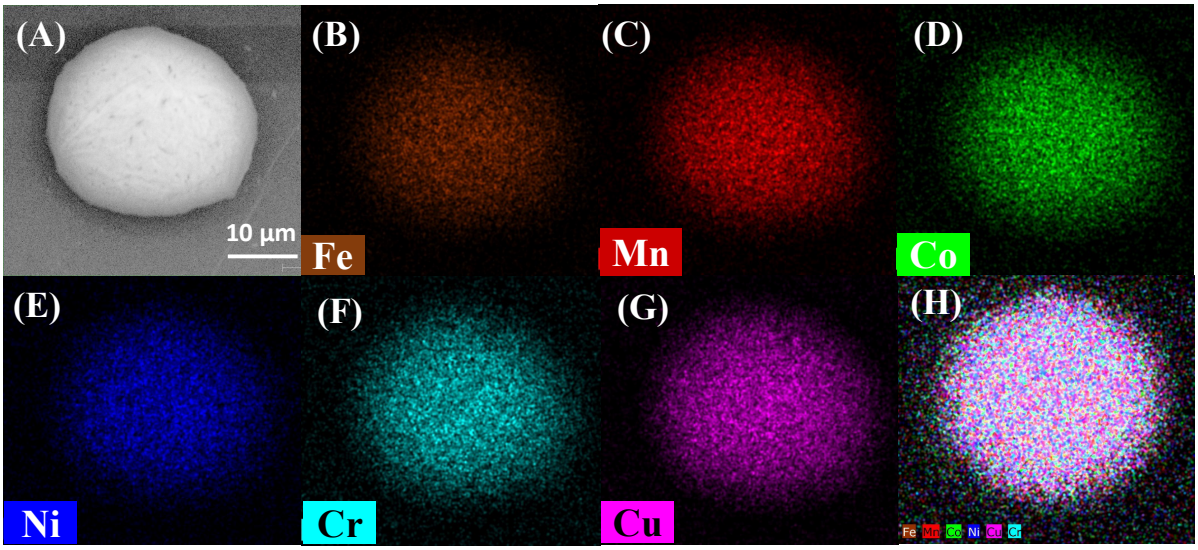

Fig. 7. SEM-EDS of the HEA particle imaged in Fig. 2 after electrochemical experiments. (A) SEM image (SE detector) of a FeCoNiCuMnCr HEA particle, (B-G) EDS elemental mapping of the same particle, and (H) the overlay of the maps shown in panels B-G.

The stability of the HEA/HOPG electrocatalyst was further assessed by bulk voltammetry. Two HEA/HOPG voltammograms (Fig. S6) were recorded before and after 5000 potential cycles between 0 and 1.8 V vs. Ag/AgCl in 0.1 M NaOH. A negligible (i.e., 8 mV) potential shift of the OER wave after 5000 potential cycles suggest that HEA/HOPG is a robust OER catalyst.

3. Conclusion

In summary, a straightforward microwave shock synthesis was carried out to produce FeCoNiCuMnCr HEA composed of six non-precious metals. The characterization of electrocatalytic activity and stability of the resulting ensemble of nanometer- to micrometer-sized HEA particles on HOPG surface is challenging because of size heterogeneity and unknown surface area of particles. SECM was used to assess electrocatalytic activity of individual HEA particles by evaluating the onset potential of OER and measuring the flux of generated oxygen at different substrate potentials. The SECM tip current was only due to oxygen reduction, thus allowing direct measurement of the OER rate at the particle unaffected by parallel processes occurring on the HEA surface. The OER current densities measured in 0.1 M NaOH are 1 mA cm^{-2} and 3 mA cm^{-2} at the 0.45 V and 0.55 V overpotential, respectively. Big differences between the OER onset potential values measured by SECM for three HEA particles and the bulk value (Fig. 4) point to significant catalytic heterogeneity of the particle population.

Several HEA particles were imaged by SEM/EDS before and after electrochemical experiments. The essentially unchanged particle size and shape and the uniform distribution of all six metals observed in SEM/EDS images obtained before and after electrochemical experiments and the lack of changes in XRD pattern suggest the apparent stability of HEA on the time scale of hours under water oxidation conditions.

4. Experimental

4.1. Materials and chemicals.

Manganese(II) chloride tetrahydrate ($MnCl_2{\cdot}4H_2O$, ⩾ 98% trace metals basis), chromium(III) chloride hexahydrate ($CrCl_3{\cdot}6H_2O$, ⩾98% trace metals basis), iron(III) chloride hexahydrate ($FeCl_3{\cdot}6H_2O$, ⩾ 98% trace metals basis), cobalt(II) chloride hexahydrate ($CoCl_2{\cdot}6H_2O$, ⩾97% trace metals basis), nickel(II) chloride hexahydrate ($NiCl_2{\cdot}6H_2O$, 99.9% trace metals basis), copper(II) chloride dihydrate ($CuCl_2{\cdot}2H_2O$, 99.999% trace metals basis), sodium hydroxide (99.999%), perchloric acid (70%, 99.999% trace metal basis), and ethanol (C_2H_5OH ⩾ 99.5%) were purchased from Sigma Aldrich, Inc. and used without further purification. Carbon paper (Sigracet, 28AA) and Toray Carbon Paper 060 (Wet Proofed) were purchased from Fuel Cell Store, Inc. ZYB grade HOPG was obtained from K-Tek nanotechnology. Aqueous solutions were prepared using deionized water from the Milli-Q Advantage A10 system equipped with Q-Gard T2 pak, a Quantum TEX cartridge, and a VOC pak; total organic carbon (TOC) <3 ppb.

4.2 Instrumentation for synthesis and characterization of HEA.

A microwave oven (Panasonic NN-SN686S, 1200 W) was used for HEA synthesis. A Branson Ultrasonic M1800 ultracentrifuge was used for centrifugation. Energy dispersive spectroscopy (EDS) was performed using an aberration-corrected JEOL ARM200CF instrument with a cold field emission gun operated at 200 kV, equipped with an Oxford X-max 100TLE windowless X-ray detector. The microstructure of the synthesized HEA/HOPG particles were characterized using scanning electron microscopy (SEM) with a Hitachi S-3600N microscope. The analysis was performed with an accelerating voltage of 30 kV in high vacuum mode. The specimen height was set to 40 mm (standard), and the working distance ranged from 12 to 14 mm. The X-ray diffraction (XRD) spectra were collected with a

PANalytical X'Pert X-ray diffractometer (Phillips, Andover, MA, USA) using CuKα (40 kV, 40 mA) radiation. The XRD patterns were recorded in the 2-theta (2θ) range from 10° to 90° at the scanning rate of 5° min^{-1}. An XE-120 AFM (Park Systems) was used for imaging the samples. Topography imaging was carried out in noncontact mode using PPP-NCHR ADM probes (Nanosensors).

4.3 Synthesis of HEA.

The surface of a 1 × 1 cm^2 HOPG substrate was peeled several times using scotch tape. To prepare FeCoNiCuMnCr HEA, equimolar amounts of chloride salts of Ni, Cr, Mn, Fe, Co, and Cu (2.5 mmol each) were dissolved together in 20 mL of ethanol. 15 µL of this solution was drop-casted onto HOPG and dried under vacuum. Salt-loaded HOPG with a piece of carbon paper on its surface was sealed in a 20 mL glass vial under vacuum. The vial was then transferred into a microwave oven, irradiated at 1200 W for 15 seconds, and naturally cooled down to room temperature. The HEA particles formed on HOPG were annealed in a furnace oven at 300 ℃ for 1 hour under Ar atmosphere inside a quartz tube to strengthen the attachment of particles to the support surface. Before sample annealing, the quartz tube was cleaned with the diluted nitric acid solution, rinsed, and pre-heated at 400 ℃ for 30 minutes.

4.4 Voltammetry

Voltammograms were obtained using a CHI600E electrochemical workstation and a three-electrode setup with an HEA-loaded HOPG, a saturated Ag/AgCl electrode, and a graphite rod serving as the working, reference, and counter electrodes, respectively. A 50 mL cell was filled with 30 mL of 0.1 M NaOH solution that was purged with Ar for 30 minutes prior to electrochemical measurements. The electrochemical activation was performed by applying five voltammetric cycles between +1.0 V and +1.80 V vs RHE with v = 50 mV/s to obtain a stable CV curve.[11] The *iR*-drop was compensated at 85%. All experiments were conducted in a Faraday cage at room temperature (23 ± 2 ºC).

2.5 Fabrication of Pt nanoelectrodes

Disk-type Pt nanoelectrodes were fabricated by pulling 25-μm-diameter annealed Pt wires (Goodfellow) into borosilicate capillaries (Drummond; OD, 1.0 mm; ID, 0.2 mm) under vacuum with a P-2000 laser puller (Sutter Instrument Co.) as described previously.[61] The pulled tips were polished on a 50 nm alumina disk (Precision Surfaces International) under video microscopic control and sonicated in deionized water for 1 min. A microforge (model MF-900, Narishige, Tokyo, Japan) was employed to reduce the RG (i.e., the ratio of glass radius to that of the conductive tip) of the tapered tip. Appropriate protective measures were used to prevent electrostatic damage to the nanoelectrodes.[62] The tip size and shape were evaluated using TEM (JEOL JEM-1400) images and SECM approach curves.

2.6 SECM Setup and Procedures

SECM experiments were carried out using a previously described home-built instrument.[63] The 4-electrode arrangement was employed with a commercial silver/silver chloride reference (CHI 111), and a 0.5 mm Pt wire serving as a counter electrode. The nanoelectrode tip was initially positioned a few tens of micrometers above a single HEA microparticle on HOPG with the help of a long-distance video microscope. A digital angle gauge (DWL-80Pro, Digi-Pas) was used to ensure the horizontal orientation of the substrate plane and the correct tip/substrate alignment. A current *vs.* distance curve was obtained during the subsequent fine approach. All experiments were conducted in a Faraday cage at room temperature (23 ± 2 ºC). The current offset of the potentiostat (~2 pA) was subtracted from all measured current values.

In the negative feedback mode, a nanotip was biased at -0.7 V vs Ag/AgCl in 0.1 M NaOH (pH = 13), while the substrate was unbiased. The nanotip was initially moved toward the HOPG surface using vertical Z piezo stage with a high approach velocity (e.g., 0.1 μm/s), which was reduced to 0.05 μm/s and then to 0.01 μm/s at shorter separation distances. To locate

a desired HEA particle, the nanotip was scanned laterally in the x-y plane over the substrate at *d* equivalent to 1-2 tip radii. The tip current was lower above HEA than above HOPG due to the blocking of O_2 diffusion by the particle surface. In the SG/TC mode, the substrate was biased at a suitable potential (between 0.2 V and 0.8 V vs. Ag/AgCl) at which no oxygen bubble formation was detected, and the potential of the Pt tip was E_T = -0.7 V.

2.7. Finite-element simulations

Simulations were carried out using COMSOL Multiphysics commercial package, version 6.1. Axisymmetric 2D models were built to simulate the SECM experiments in the negative feedback and SG/TC modes. The "transport of dilute species" model was used to solve steady-state diffusion problems. The COMSOL modeling report is available in Supplementary Information.

Data availability

The data supporting this article have been included as part of the supplementary information.

Conflicts of interest

There are no conflicts to declare.

Acknowledgments

The support of this work by the National Science Foundation grant CHE-2406702 is gratefully acknowledged.

Footnotes

Electronic supplementary information (ESI) available. See DOI: https://doi.org/10.1039/

References

1 T. A. A. Batchelor, J. K. Pedersen, S. H. Winther, I. E. Castelli, K. W. Jacobsen and J. Rossmeisl, High-Entropy Alloys as a Discovery Platform for Electrocatalysis, *Joule*, 2019, **3**, 834-845.

2 Y. Yao, Q. Dong, A. Brozena, J. Luo, J. Miao, M. Chi, C. Wang, I. G. Kevrekidis, Z. J. Ren, J. Greeley, G. Wang, A. Anapolsky and L. Hu, High-entropy nanoparticles: synthesis-structure-property relationships and data-driven discovery, *Science*, 2022, **376**, eabn3103.

3 Y. Sun and S. Dai, High-entropy materials for catalysis: A new frontier, *Sci. Adv.*, 2021, **7**,eabg1600.
4 Y. Nakaya and S. Furukawa, High-entropy intermetallics: emerging inorganic materials for designing high-performance catalysts, *Chem. Sci.*, 2024, **15**, 12644-12666.
5 F. Marques, M. Balcerzak, F. Winkelmann, G. Zepon and M. Felderhoff, Review and outlook on high-entropy alloys for hydrogen storage, *Energy Environ. Sci.*, 2021, **14**, 5191-5227.
6 D. B. Miracle and O. N. Senkov, A critical review of high entropy alloys and related concepts, *Acta Materialia*, 2017, **122**, 448-511.
7 E. P. George, D. Raabe and R. O. Ritchie, High-entropy alloys, *Nat. Rev. Mater.*, 2019, **4**, 515-534.
8 Y. Xin, S. Li, Y. Qian, W. Zhu, H. Yuan, P. Jiang, R. Guo and L. Wang, High-Entropy Alloys as a Platform for Catalysis: Progress, Challenges, and Opportunities, *ACS Catal.*, 2020, **10**, 11280-11306.
9 Y. Sun and S. Dai, High-entropy materials for catalysis: A new frontier, *Sci. Adv.*, 2021, **7**, eabg1600.
10 A. Amiri and R. Shahbazian-Yassar, Recent progress of high-entropy materials for energy storage and conversion, *J. Mat. Chem. A*, 2021, **9**, 782-823.
11 A. L. Maulana, P. C. Chen, Z. Shi, Y. Yang, C. Lizandara-Pueyo, F. Seeler, H.D. Abruña, D. Muller, K. Schierle-Arndt and P. Yang, Understanding the Structural Evolution of IrFeCoNiCu High-Entropy Alloy Nanoparticles under the Acidic Oxygen Evolution Reaction, *Nano Lett.*, 2023, **23**, 6637-6644.
12 X. Zhao, H. Cheng, X. Chen, Q. Zhang, C. Li, J. Xie, N. Marinkovic, L. Ma, J. C. Zheng and K. Sasaki, Multiple Metal–Nitrogen Bonds Synergistically Boosting the Activity and Durability of High-Entropy Alloy Electrocatalysts, *J. Am. Chem. Soc.*, 2024, **146**, 3010-3022.
13 S. Bolar, Y. Ito and T. Fujita, Future prospects of high-entropy alloys as next-generation industrial electrode materials, *Chem. Sci.*, 2024, **15**, 8664-8722.
14 L. Banko, O. A. Krysiak, J. K. Pedersen, B. Xiao, A. Savan, T. Löffler, S. Baha, J. Rossmeisl, W. Schuhmann and A. Ludwig, Unravelling Composition–Activity–Stability Trends in High Entropy Alloy Electrocatalysts by Using a Data-Guided Combinatorial Synthesis Strategy and Computational Modeling, *Adv. Energy Mater.*, 2022, **12**, 2103312.
15 J. Liang, G. Cao, M. Zeng and L. Fu, Controllable synthesis of high-entropy alloys, *Chem. Soc. Rev.*, 2024, **53**, 6021-6041
16 Y. Liu, C. Hsieh, L. Hsu, K. Lin, Y. Hsiao, C. Chi, J. Lin, C. Chang, S. Lin, C. Wu, J. Gao, C. Pao, Y. Chang, M. Lu, S. Zhou and T. Yang, Toward controllable and predictable synthesis of high-entropy alloy nanocrystals, *Sci. Adv.*, 2023, **9**, eadf9931.
17. R. He, L. Yang, Y. Zhang, D. Jiang, S. Lee, S. Horta, Z. Liang, X. Lu, A. Ostovari Moghaddam, J. Li, M. Ibáñez, Y. Xu, Y. Zhou and A. Cabot, A 3d-4d-5d High Entropy Alloy as a Bifunctional Oxygen Catalyst for Robust Aqueous Zinc–Air Batteries, *Adv. Mater.*,2023, **35**, 2303719.
18 M. Liu, Z. Zhang, F. Okejiri, S. Yang, S. Zhou and S. Dai, Entropy-Maximized Synthesis of Multimetallic Nanoparticle Catalysts via a Ultrasonication-Assisted Wet Chemistry Method under Ambient Conditions, *Adv. Mater. Interfaces*, 2019, **6**, 1900015.
19 P. Chen, X. Liu, J. Hedrick, Z. Xie, S. Wang, Q. Lin, M. C. Hersam, V. P. Dravid and C. A. Mirkin, Polyelemental nanoparticle libraries, *Science*, 2016, **352**, 1565-1569.
20 S. Wu, Y. Liu, Y. Ren, Q. Wei and Y. Sun, Microwave synthesis of single-phase nanoparticles made of multi-principal element alloys, *Nano Res.*, 2022, **15**, 4886–4892.

21 Y. Yang, B. Song, X. Ke, F. Xu, K. N. Bozhilov, L. Hu, R. Shahbazian-Yassar and M. R. Zachariah, Aerosol Synthesis of High Entropy Alloy Nanoparticles, *Langmuir*, 2020, **36**, 1985-1992.
22 Y. Yao, Z. Huang, P. Xie, S. D. Lacey, R. J. Jacob, H. Xie, F. Chen, A. Nie, T. Pu, M. Rehwoldt, D. Yu, M. R. Zachariah, C. Wang, R. Shahbazian-Yassar, J. Li and L. Hu, Carbothermal shock synthesis of high-entropy-alloy nanoparticles, *Science*, 2018, **359**, 1489-1494.
23 S. Gao, S. Hao, Z. Huang, Y. Yuan, S. Han, L. Lei, X. Zhang, R. Shahbazian-Yassar and J. Lu, Synthesis of high-entropy alloy nanoparticles on supports by the fast moving bed pyrolysis, *Nat. Commun.*, 2020, **11**, 2016.
24 Y. Yao, Z. Liu, P. Xie, Z. Huang, T. Li, D. Morris, Z. Finfrock, J. Zhou, M. Jiao, J. Gao, Y. Mao, J. Miao, P. Zhang, R. Shahbazian-Yassar, C. Wang, G. Wang and L. Hu, Computationally aided, entropy-driven synthesis of highly efficient and durable multi-elemental alloy catalysts, *Sci. Adv.*, 2020, **6** eaaz0510.
25 Y. Yang, B. Song, X. Ke, F. Xu, K. Bozhilov, L. Hu, R. Shahbazian-Yassar, M. Zachariah, Aerosol Synthesis of High Entropy Alloy Nanoparticles. *Langmuir* 2020, **36**, 1985.
26 H. Qiao, M.T. Saray, X. Wang, S. Xu, G. Chen, Z. Huang, C. Chen, G. Zhong, Q. Dong, M. Hong, H. Xie, R. Shahbazian-Yassar and L. Hu, Scalable Synthesis of High Entropy Alloy Nanoparticles by Microwave Heating, *ACS Nano*, 2021, **15**, 14928-14937.
27 W. Zhu, X. Gao, Y. Yao, S. Hu, Z. Li, Y. Teng, H. Wang, H. Gong, Z. Chen and Y. Yang, Nanostructured High Entropy Alloys as Structural and Functional Materials, *ACS Nano*, 2024, **18**, 12672-12706.
28 Y. Huang, D. Wang, Y. Yu, Z. Li, X. Wen and Z. Wang, High-Entropy Oxides as Electrocatalysts for the Oxygen Evolution Reaction: A Mini Review, *Energy & Fuels*, 2024, **38**, 13661-13684.
29 J. Baek, M. D. Hossain, P. Mukherjee, J. Lee, K. T. Winther, J. Leem, Y. Jiang, W. C. Chueh, M. Bajdich and X. Zheng, Synergistic effects of mixing and strain in high entropy spinel oxides for oxygen evolution reaction, *Nat. Commun*, 2023, **14**, 5936.
30 Y. Lee, J. Suntivich, K. J. May, E. E. Perry and Y. Shao-Horn, Synthesis and Activities of Rutile IrO_2 and RuO_2 Nanoparticles for Oxygen Evolution in Acid and Alkaline Solutions, *J. Phys. Chem. Lett.*, 2012, **3**, 399-404.
31 X. Li, X. Hao, A. Abudula and G. Guan, Nanostructured catalysts for electrochemical water splitting: current state and prospects, *J. Mater. Chem. A*, 2016, **4**, 11973-12000.
32 S. Trasatti, Electrocatalysis by oxides — Attempt at a unifying approach, *J. Electroanal. Chem. Interfacial Electrochem.*, 1980, **111**, 125-131.
33 C. Cai, Z. Xin, X. Zhang, J. Cui, H. Lv, W. Ren, C. Gao and B. Cai, Facile Synthesis of FeCoNiCuIr High Entropy Alloy Nanoparticles for Efficient Oxygen Evolution Electrocatalysis, *Catalysts*, 2022, **12**, 1050
34 V.A. Mints, K.L. Svane, J. Rossmeisl and M. Arenz, Exploring the High-Entropy Oxide Composition Space: Insights through Comparing Experimental with Theoretical Models for the Oxygen Evolution Reaction, *ACS Catal.*, 2024, **14**, 6936-6944.
35 J. Hao, Z. Zhuang, K. Cao, G. Gao, C. Wang, F. Lai, S. Lu, P. Ma, W. Dong, T. Liu, M. Du and H. Zhu, Unraveling the electronegativity-dominated intermediate adsorption on high-entropy alloy electrocatalysts, *Nat. Commun.*, 2022, **13**, 2662.
36 K. L. Svane and J. Rossmeisl, Theoretical Optimization of Compositions of High-Entropy Oxides for the Oxygen Evolution Reaction, *Angew. Chem. Int. Ed.*, 2022, **61**, e202201146.
37 Z.W. Seh, J. Kibsgaard, C. F. Dickens, I. Chorkendorff, J. K. Nørskov and T. F. Jaramillo, Combining theory and experiment in electrocatalysis: Insights into materials design, *Science*, 2017, **355**, eaad4998.

38 L. An, C. Wei, M. Lu, H. Liu, Y. Chen, G. G. Scherer, A. C. Fisher, P. Xi, Z. Xu and C. Yan, Recent Development of Oxygen Evolution Electrocatalysts in Acidic Environment, *Adv. Mater.*, 2021, **33**, 2006328.
39 S. A. Lee, J. Bu, J. Lee and H. W. Jang, High-Entropy Nanomaterials for Advanced Electrocatalysis, *Small Sci.*, 2023, **3**, 2200109.
40 R. He, L. Yang, Y. Zhang, X. Wang, S. Lee, T. Zhang, L. Li, Z. Liang, J. Chen, J. Li, A. Ostovari Moghaddam, J. Llorca, M. Ibáñez, J. Arbiol, Y. Xu and A. Cabot, A CrMnFeCoNi high entropy alloy boosting oxygen evolution/reduction reactions and zinc-air battery performance, *Energy Storage Mater.*, 2023, **58**, 287-298.
41 B. Nourmohammadi Khiarak, M. Mojaddami, Z. Zamani Faradonbeh, A. O. Zekiy, and A. Simchi, Efficient Electrocatalytic Overall Water Splitting on a Copper-Rich Alloy: An Electrochemical Study, *Energy & Fuels*, 2022, **36**, 4502-4509.
42 M. Li, F. Lin, S. Zhang, R. Zhao, L. Tao, L. Li, J. Li, L. Zeng, M. Luo and S. Guo, High-entropy alloy electrocatalysts go to (sub-)nanoscale, *Sci. Adv.*, 2024, **10** eadn2877.
43 T. Priamushko, A. Kormányos and S. Cherevko, What do we know about the electrochemical stability of high-entropy alloys?, *Curr. Opin. Chem. Eng.*, 2024, **44**, 101020.
44 X. He, Z. Zhang, X. Jiang, H. Liu, T. Xing and X. Wang, Carbon cloth supporting $(CrMnFeCoCu)_3O_4$ high entropy oxide as electrocatalyst for efficient oxygen evolution reactions, *J. Alloys Compd.*, 2024, **1004**, 175874.
45 F. D. Speck, A. Zagalskaya, V. Alexandrov and S. Cherevko, Periodicity in the Electrochemical Dissolution of Transition Metals, *Angew. Chem. Int. Ed.*, 2021, **60**, 13343-13349.
46 B. Song, Y. Yang, M. Rabbani, T. T. Yang, K. He, X. Hu, Y. Yuan, P. Ghildiyal, V. P. Dravid, M. R. Zachariah, W. A. Saidi, Y. Liu and R. Shahbazian-Yassar, In Situ Oxidation Studies of High-Entropy Alloy Nanoparticles, *ACS Nano*, 2020, **14**, 15131-15143.
47 A. Kormányos, Q. Dong, B. Xiao, T. Li, A. Savan, K. Jenewein, T. Priamushko, A. Körner, T. Böhm, A. Hutzler, L. Hu, A. Ludwig and S. Cherevko, Stability of high-entropy alloys under electrocatalytic conditions, *iScience*, 2023, **26**, 107775.
48 L. Sun, K. Wen, G. Li, X. Zhang, X. Zeng, B. Johannessen and S. Zhang, High-Entropy Alloys in Catalysis: Progress, Challenges, and Prospects, *ACS Mater. Au*, 2024, **4**, 547-556 .
49 J. L. Fernández, D. A. Walsh and A. J. Bard, Thermodynamic Guidelines for the Design of Bimetallic Catalysts for Oxygen Electroreduction and Rapid Screening by Scanning Electrochemical Microscopy. M−Co (M: Pd, Ag, Au). *J. Am. Chem. Soc.* 2005, **127**, 357–365.
50 A. Minguzzi, D. Battistel, J. Rodríguez-López, A. Vertova, S. Rondinini, A. J. Bard and S. Daniele, Rapid Characterization of Oxygen-Evolving Electrocatalyst Spot Arrays by the Substrate Generation/Tip Collection Mode of Scanning ElectrochemicalMicroscopy with Decreased O_2 Diffusion Layer Overlap. *J. Phys.Chem. C*, 2015, **119**, 2941−2947.
51 H. S. Ahn and A. J. Bard, Surface interrogation scanning electrochemical microscopy of Ni1– x Fex OOH (0 < x < 0.27) oxygen evolving catalyst: Kinetics of the “Fast” iron sites. *J. Am. Chem. Soc.* 2016, **138**, 313–318.
52 J. M. Barforoush, T. E. Seuferling, D. T. Jantz, K. R. Song and K. C. Leonard, Insights into the Active Electrocatalytic Areas of Layered Double Hydroxide and Amorphous Nickel−Iron Oxide Oxygen Evolution Electrocatalysts. *ACS Appl. Energy Mater.* 2018, **1**, 1415−1423.
53 M. Kim, E. B. Tetteh, O. A. Krysiak, A. Savan, B. Xiao, T. H. Piotrowiak, C. Andronescu, A. Ludwig, T. D. Chung and W. Schuhmann, Acidic hydrogen evolution electrocatalysis

at high-entropy alloys correlates with its composition - dependent potential of Zerocharge. *Angew Chem. Int. Ed.,* 2023, **62**, e202310069.
54 E. B. Tetteh, O. A. Krysiak, A. Savan, M. Kim, R. Zerdoumi, T. D. Chung and A. Ludwig, W. Schuhmann, Long-Range SECCM Enables High-Throughput Electrochemical Screening of High Entropy Alloy Electrocatalysts at Up-To-Industrial Current Densities. *Small Methods*, 2024, **8**, 2301284.
55 H. S. Ahn, C. G. Zoski and A. J. Bard, Electrocatalysis and Surface Interrogation. In Scanning Electrochemical Microscopy, 3rd ed., (A. J. Bard and M. V. Mirkin,, Eds.) *CRC Press: Boca Raton*, 2022, 127–153.
56 S. Xu, G. Zhong, C. Chen, M. Zhou, D. J. Kline, R. J. Jacob, H. Xie, S. He, Z. Huang, J. Dai, A. H. Brozena, R. Shahbazian-Yassar, M. R. Zachariah, S. M. Anlage and L. Hu, Uniform, Scalable, High-Temperature Microwave Shock for Nanoparticle Synthesis through Defect Engineering, *Matter*, 2019, **1**, 759-769.
57 G. Zhong, S. Xu, M. Cui, Q. Dong, X. Wang, Q. Xia, J. Gao, Y. Pei, Y. Qiao, G. Pastel, T. Sunaoshi, B. Yang and L. Hu, Rapid, High-Temperature, In Situ Microwave Synthesis of Bulk Nanocatalysts, *Small*, 2019, **15**, 1904881.
58 R. J. Jacob, D. J. Kline and M. R. Zachariah, High speed 2-dimensional temperature measurements of nanothermite composites: Probing thermal vs. Gas generation effects, *J. Appl. Phys.*, 2018, **123**, 115902.
59 L. Ngoc, K. Kang, G. Choi, The measurement of anisotropic thermal transport using time-resolved magneto-optical Kerr effect. AIP Adv., 2021, **11**, 025024.
60 K. Barman, G. Askarova, R. Jia, G. Hu and M. V. Mirkin, Efficient Voltage-Driven Oxidation of Water and Alcohols by Organic Molecular Catalyst Directly Attached to a Carbon Electrode. *J. Am. Chem. Soc.* 2023*,* **145**, 5786−5794.
61 P. Sun and M.V. Mirkin, Kinetics of Electron-Transfer Reactions at Nanoelectrodes, *Anal. Chem.*, 2006, **78**, 6526-6534.
62 N. Nioradze, R. Chen, J. Kim, M. Shen, P. Santhosh and S. Amemiya, Origins of Nanoscale Damage to Glass-Sealed Platinum Electrodes with Submicrometer and Nanometer Size, *Anal. Chem.*, 2013, **85**, 6198-6202.
63 T. Bo, X. Wang, R. Jia, L. Han, H.L. Xin, H. Zhang, E.M. Miller, M.V. Mirkin, Probing Activities of Individual Catalytic Nanoflakes by Tunneling Mode of Scanning Electrochemical Microscopy, *J. Phys. Chem. C*, 2021, **125**, 25525-25532.